SCIENTIFIC REPORTS

OPEN

A micro-Raman study of exfoliated few-layered *n*-type Bi$_2$Te$_{2.7}$Se$_{0.3}$

Fengjiao Liu[1], Longyu Hu[2], Mehmet Karakaya[1], Pooja Puneet[1], Rahul Rao[3,4], Ramakrishna Podila[1,5], Sriparna Bhattacharya[1] & Apparao M. Rao[1,5]

Previously we showed that the thermoelectric (TE) performance of bulk *n*-type Bi$_2$Te$_{2.7}$Se$_{0.3}$ can be enhanced by subjecting it to a combined process of chemical or mechanical exfoliation (C/ME) followed by a rapid densification and restacking of the exfoliated layers via the spark-plasma-sintering technique (SPS). Here, we present a systematic micro-Raman study of two-dimensional flakes of *n*-type Bi$_2$Te$_{2.7}$Se$_{0.3}$ produced by the C/ME process, as a function of the flake thickness. We found Raman evidence for flakes with: (i) integer number of quintuples which exhibited a strong electron-phonon coupling, and (ii) non-integer number of quintuples, or sub-quintuples which exhibited the forbidden IR active mode due to symmetry lowering. Detailed atomic force microscopy was used to confirm the number of quintuples in all flakes examined in this study. The restacking and densification of these flakes by SPS promoted the formation of charged grain boundaries, which led to the enhanced TE properties via the energy filtering process.

Bulk pristine (undoped) and doped Bi$_2$Te$_3$ are some of the most efficient room temperature thermoelectric (TE) materials for sustainable power generation and refrigeration applications[1–3]. The efficiency of a TE material is determined by its dimensionless figure of merit, $ZT = \alpha^2\sigma T/\kappa$, where α is Seebeck coefficient or thermopower, σ is electrical conductivity, and $\kappa(=\kappa_E + \kappa_L)$ is the total thermal conductivity, which is comprised of electronic and lattice contributions, respectively. The main challenge for improving ZT of any TE material is the inherent coupling between α, σ, and κ that prevents increased α and σ with a concomitant decrease in κ. Bi$_2$Te$_3$ is also of tremendous interest as a topological insulator (TI), which in turn is promising for TE energy conversion[4–6]. In contrast to ordinary materials, backscattering of electrons due to collisions with impurities and defects in the crystal lattice is completely suppressed on the surfaces of TIs, giving rise to improved charge transfer and mobility, and thus enhanced σ. The existence of surface states in TIs arise from the intrinsic spin-orbit coupling that is enhanced with increasing atomic masses, which can also increase the mass fluctuation scattering effect to reduce κ_L. It is thus observed that most topological insulators such as Bi$_2$Te$_3$, Bi$_2$Se$_3$, exhibit excellent TE properties.

In the 1990s, Hicks and Dresselhaus predicted that an increase in the density of states could lead to enhanced α[7]. In addition to improving electronic transport in low dimensional materials, nanostructuring via ball-milling and melt-spinning have been effective in reducing κ_L through increased phonon scattering effects, resulting in an enhanced ZT in TE nanomaterials[8,9]. In recent years, chemical/mechanical exfoliation (C/ME) of layered materials has enabled the fabrication of two-dimensional (2D) nanosheets that exhibit superior TE properties compared to their bulk counterparts[10–14].

Bulk Bi$_2$Te$_3$ exhibits a layered crystal structure and its conventional unit cell is comprised of three quintuples. Each quintuple contains five atomic layers with a sequence of Te^1-Bi-Te^2-Bi-Te^1 called quintuple layers (QL), and the weak van der Waals bond between Te^1-Te^1 couples the quintuples together[15]. Therefore during the C/ME process, the Te^1-Te^1 bond between the QLs can be broken, giving rise to unique optical and electronic transport, compared to the bulk[16,17]. Previously we employed the combined technique of C/ME followed by spark-plasma-sintering (SPS), which led to preferential scattering of electrons at charged grain boundaries, and significantly improved the TE compatibility factor and stabilized the ZT peak at higher temperatures (350–500 K) in *n*-type Bi$_2$Te$_{2.7}$Se$_{0.3}$[10]. The C/ME-SPS process resulted in two important contributions: (i) an increase in the electrical conductivity due to an increase in carrier concentration despite the presence of numerous grain boundaries, and (ii) the mitigation of the bipolar effect via band occupancy optimization which led to an upshift and

[1]Clemson Nanomaterials Institute, Department of Physics & Astronomy, Clemson University, Clemson, 29634, SC, USA. [2]Department of Chemistry, Clemson University, Clemson, SC, 29634, USA. [3]Materials and Manufacturing Directorate, Air Force Research Laboratory, WPAFB, Dayton, OH, 45433, USA. [4]UES Inc., Dayton, OH, 45432, USA. [5]Laboratory of Nano-biophysics, Clemson University, Clemson, SC, 29634, USA. Correspondence and requests for materials should be addressed to R.R. (email: Rahul.rao.ctr.in@us.af.mil) or S.B. (email: bbhatta@clemson.edu)
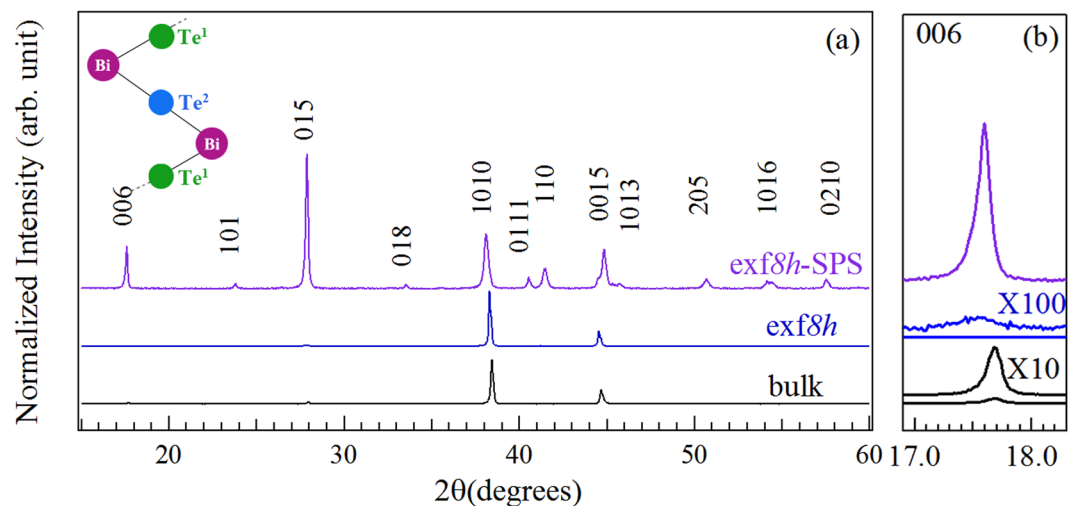
    1

Figure 1. X-ray diffraction patterns. (**a**) Bulk n-type $Bi_2Te_{2.7}Se_{0.3}$ sample compared to the 8-hr exfoliated flake before and after SPS with a Bi_2Te_3 quintuple as inset; (**b**) (006) peak suppressed in the exf8h (X100), but more pronounced in the exf8h-SPS.

stabilization of the ZT peak over a broad temperature range of $\sim150\,K$[10]. Both (i) and (ii) implied the creation of charged grain boundaries in $Bi_2Te_{2.7}Se_{0.3}$ due to the C/ME-SPS process.

To understand the structural changes in the $Bi_2Te_{2.7}Se_{0.3}$ brought about by the C/ME process, we performed a detailed micro-Raman study of C/ME n-type $Bi_2Te_{2.7}Se_{0.3}$ with varying layer thicknesses down to $\sim2\,nm$ (~2 quintuples). To the best of our knowledge, previous Raman studies of bulk and few-layered Bi_2Te_3 delineated the Raman-active modes in pristine Bi_2Te_3, and the effect of Se doping in the chemically exfoliated layers was still largely ignored. Our transport measurements were performed on the exfnh-SPS samples (exfnh, where n represents the exfoliation time in hours) and showed a decrease in electrical resistivity concomitant with an increase in carrier concentration, thereby resulting in a lower Seebeck coefficient. Moreover, we found a decrease in thermal conductivity with decreasing layer thickness. Micro-Raman measurements on the C/ME samples revealed the co-existence of whole quintuples with strong surface states (electron-phonon coupling) and sub-quintuples that exhibited forbidden (IR-active) modes in the Raman spectra. The combination of these two "phases" results in the formation of charged grain boundaries upon SPS-processing and thus enhanced TE performance.

Results and Discussion

Bulk Bi_2Te_3 exhibits a trigonal crystal structure belonging to the space group $R\bar{3}m$[18], but is more commonly represented by a hexagonal crystal structure (see Supplementary Fig. S1). The highly anisotropic hexagonal unit cell consists of three quintuples each consisting of five atoms, stacked in the order Te^1-Bi-Te^2-Bi-Te^1 along the c-axis, with lattice constants $a = 4.38\,Å$ and $c = 30.36\,Å$[1]. Each quintuple measures approximately $1\,nm$ across the five atoms. The quintuples are held together by weak van der Waals forces (Te^1-Te^1 bond) corresponding to the largest spacing $d \sim 0.37\,nm$[16] that make them easily cleavable. In general, for $Bi_2Te_{3-x}Se_x$ the Se atoms preferentially replace Te at Te^2 sites first and then randomly replace Te at the Te^1 sites[14,19]. With Se-doping at the Te^2 sites, a breakdown of the $Bi_2Te_{2.7}Se_{0.3}$ quintuples into bi-layer or tri-layer sub-quintuples (e.g., Bi-Te^1, Te^1-Bi-Te^2, Te^1-Bi-Se^2) during the C/ME process is feasible because the Bi-Te^1 bond strength is the strongest bond in the quintuple[20]. In addition, the Te^2 atom is known to lie at the inversion center of the D_{3d}^5 symmetry[21], and hence the Se doping can change the crystalline structure as well as the lattice dynamics in a unique manner.

Figure 1a shows the powder HR-XRD patterns of the bulk compared to that of the exf8h and exf8h-SPS samples. Both XRD patterns are consistent with the expected pattern for $Bi_2Te_{2.7}Se_{0.3}$ (JCPDS card no. 00-050-0954). The (006) peak (Fig. 1b) was severely broadened in the data of the exf8h sample (inferred by magnifying it a 100 fold) due to nano-structuring and bond cleavages at various locations along the c-direction, while it became more pronounced after SPS treatment, suggesting an improvement in the coherence length. The representative TEM and AFM images (Fig. 2a and b) of the exf8h samples show lateral sizes ranging from $\sim0.3\,\mu m$ to $0.8\,\mu m$ and a height of $\sim2\,nm$ (Fig. 2d). The roughness (R_q)[22] of this representative AFM image is about $0.1\,nm$. The average thickness of the n-type $Bi_2Te_{2.7}Se_{0.3}$ layers as a function of the exfoliation time is shown in Fig. 2c. With an increase in the exfoliation time, the layer thickness t of the $Bi_2Te_{2.7}Se_{0.3}$ decreased significantly between the exfoliation times of 0 to 3 hr, down to $\sim1.6\,nm$ after 8 hr exfoliation. Further exfoliation time did not significantly reduce the thickness of the flakes. The presence of sub-quintuples was evidenced from the non-integer values of t from AFM linescans of the flakes, since $1\,nm$ corresponds to one quintuple as discussed above.

Figure 3 shows the thermoelectric transport properties of the exfnh-SPS samples compared to the bulk sample. The electrical resistivity ($\rho = 1/\sigma$) increased linearly with increasing temperature (Fig. 3a), indicating a "metal-like" or degenerate semiconducting behavior. A slight change of slope was observed in the bulk sample at $\sim360\,K$, consistent with the upturn in α (Fig. 3c) due to the bipolar effect. With increasing exfoliation time, the ρ values in the exfnh-SPS samples were consistently lower than the corresponding value in the bulk due to increase
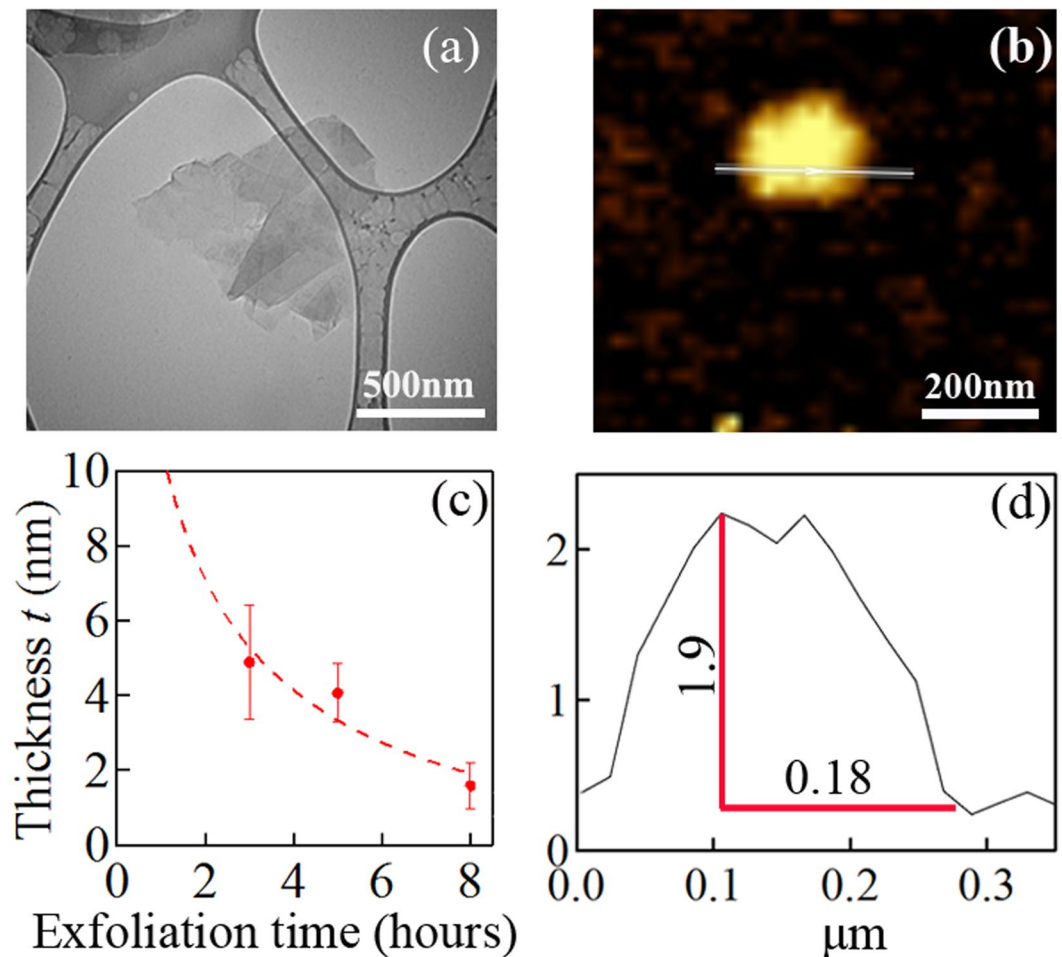
Figure 2. Representative TEM (**a**) and AFM (**b**) images of the exf8h sample. (**c**) The average thickness of the exfoliated n-type $Bi_2Te_{2.7}Se_{0.3}$ flakes as a function of exfoliation times (0 h, 3 h, 5 h, and 8 h). The full width of half maximum of thickness distribution (Gaussian distribution) were used as error bars. t tends to be infinite at 0 h and the dash line is a guide to the eye. (**d**) The lateral size and height of a representative flake shown in (**b**).

in the carrier concentration n (Fig. 3b inset). The carrier mobility $\mu = 1/ne\rho$, where e is the electron charge, (Fig. 3b) also exhibited a reduction with increased exfoliation times at temperatures below 100 K where the grain boundary and charged defect scattering dominates. Puneet et al. attributed the increase in n to selective filtering of charge carriers by positively charged grain boundaries resulting from Te_{Bi} anti-site and bismuth vacancies (V_{Bi} defects)[10,16].

The Seebeck coefficient or thermopower (α) of the bulk $Bi_2Te_{2.7}Se_{0.3}$ sample (Fig. 3c) exhibited a high negative value (~200 μV/K) at 300 K, while α in the exfnh-SPS samples reduced to 130~170 μV/K (65~85% of the bulk value), which is consistent with the reduction of ρ due to increase in n, as α varies as $n^{-2/3}$ shown in equation (1). Using a simple parabolic band approximation, the effective masses (m^*) of the charge carriers in exfnh-SPS samples were calculated from the measured α and n values at room temperature using the relation[23,24].

$$\alpha = \left(\frac{8\pi^2 k_B^2}{3eh^2}\right) m^* T \left(\frac{\pi}{3n}\right)^{(2/3)} \tag{1}$$

where k_B is the Boltzmann constant, e the electronic charge, and h the Planck's constant. The effective masses (m^*) for the bulk and exfnh samples, estimated from α vs. n at 300 K (Pisarenko plot, Fig. 3c inset) were found to be ~0.95 m_e, where m_e is the mass of the electron. In addition, the band gaps (E_g) of the exfoliated samples estimated using the Goldsmid Sharp relation[25]:

$$E_g = 2e\alpha_{max}T_{max} \tag{2}$$

remained constant ~0.16 eV (see Supplementary Table S1) which are consistent with the reported values[1]. This indicates that the systematic reductions in α with increasing exfoliation times could be solely attributed to increasing n (inset, Fig. 3b) and not from changes in band gap or band curvature. With increasing temperature, $|\alpha|$ of the bulk sample increased till α_{max} was reached, above which the bipolar (two carrier) effect was observed. Specifically, $|\alpha|$ decreased as indicated by the upturn at T = 362 K in Fig. 3c, which is typical of a narrow band
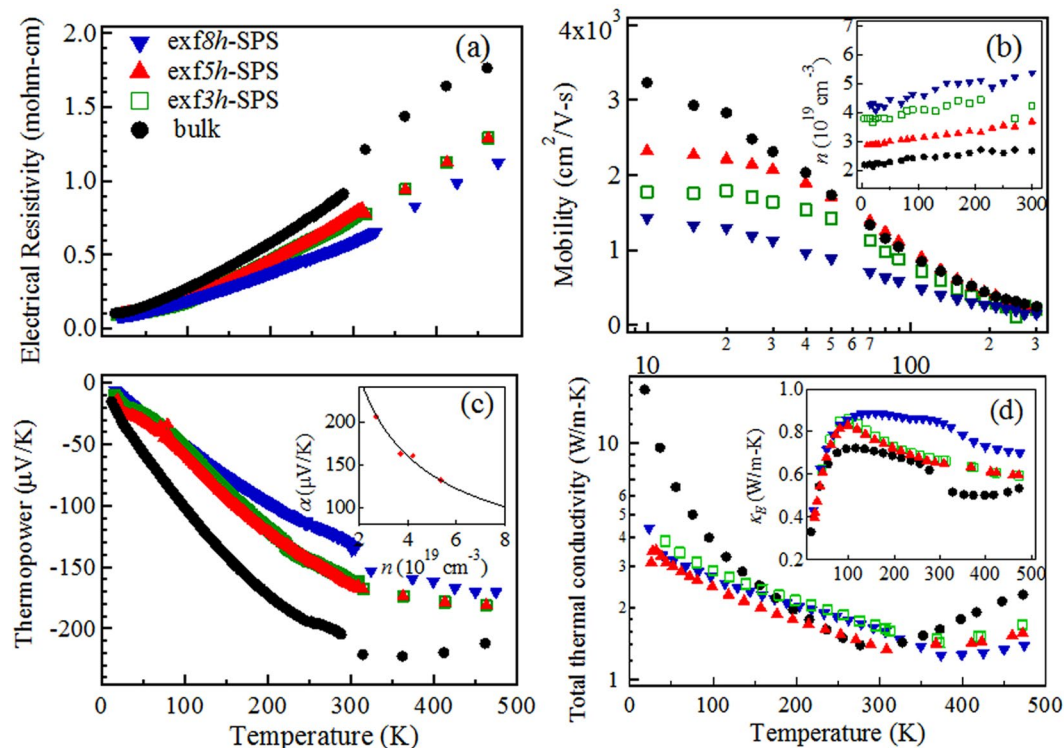
Figure 3. Temperature dependence of transport properties. (**a**) The electrical resistivity (ρ); (**b**) mobility (μ) with carrier concentration (n) as inset; (**c**) temperature dependence of the Seebeck coefficient (α) with its dependence on carrier concentration shown in the inset; (**d**) total thermal conductivity (κ) with electronic thermal conductivity (κ_E) as inset of the exf3h-SPS, exf5h-SPS, exf8h-SPS samples as a function of temperature compared to the bulk sample.

gap semiconductor. As concluded by Puneet et al. the low energy minority carriers in the exf8h samples were selectively filtered due to the presence of the positively charged defects on the grain boundary (interfacial charged defects) which upshifted the α_{max} to above 500 K[10]. With the reduction of the bipolar term, this upshift in α_{max} led to the broadening of ZT in the exfnh-SPS samples as shown in Supplementary Fig. S2.

The presence of grain boundary potential barrier scattering in the n-type $Bi_2Te_{2.7}Se_{0.3}$ samples is evidenced from the temperature dependence of σ, where $\sigma \sim T^{-1/2}\exp(\frac{-E_B}{kT})$[26] and the associated grain boundary potential barrier height (E_B) was calculated from the linear plot of $ln(\sigma T^{1/2})$ vs. $1/kT$ as shown in Supplementary Fig. S3. As expected, the exfnh-SPS samples exhibited higher $E_B \sim 23$–27 meV arising from the increased number of grain boundaries (grain size $\sim 20 \mu$ m) compared to the $E_B \sim 19$ meV of the ingot that exhibited relatively larger grains. For comparison, an $E_B \sim 60$ meV was reported in PbTe nanocomposites, wherein grain boundary potential barrier scattering is known to be a dominant scattering mechanism[27]. Furthermore, evidence for the presence of charged grain boundaries in n-type $Bi_2Te_{2.7}Se_{0.3}$ samples was also found using Kelvin probe Force Microscopy (KPFM; Supplementary Fig. S4) as detailed in the SI section.

The bulk sample exhibited a high magnitude of total thermal conductivity (κ) at ~ 17 K as shown in Fig. 3d, which decreased subsequently in the exfnh-SPS samples due to exfoliation-induced disorder. A well-defined peak is expected at lower temperatures in the bulk sample (indicating good crystal quality), before κ decreased with increasing temperature due to anharmonic phonon-phonon or Umklapp scattering effects. At ~ 360 K, κ increased gradually with increasing temperature, due to contribution from the bipolar effect. The inset showed the systematic increase in κ_E ($=L_0\sigma T$) (where L_0 is the Lorenz number, $L_0 = 1.66 \times 10^{-8}$ V^2/K^2 for the nanostructured samples[28]) in the exfnh-SPS samples compared to the bulk, indicating that $\kappa_T - \kappa_E$ was also reduced due to increased phonon scattering at the grain boundaries. The bipolar contribution however was absent and possibly shifted to higher temperatures in the exfoliated samples. Taken together, the plots in Fig. 3 show that the C/ME-SPS treatment of n-type resulted in: i) an increase (decrease) in carrier concentration (resistivity), ii) mitigation of the bipolar effect in thermopower, and iii) a simultaneous reduction in the thermal conductivity, that led to the broadening of the ZT peak over a wider range of temperature ~ 100 K (see Supplementary Fig. S2).

To gain more understanding into the structural properties underpinning the unique TE performance of the exfoliated samples, we used micro-Raman spectroscopy, which is an ideal technique for studying the changes in the vibrational (and hence TE) properties caused by the C/ME process in n-type $Bi_2Te_{2.7}Se_{0.3}$. Micro-Raman spectra were collected from several different spots on the bulk, exf3h, exf5h and exf8h $Bi_2Te_{2.7}Se_{0.3}$ samples. Upon densifying these samples using SPS, the SPS-compacted samples exhibited a high background making them unsuitable for Raman studies. Nevertheless, significant structural changes in the exfoliated layers due to the C/ME process were evident in our micro-Raman spectra, as discussed below.
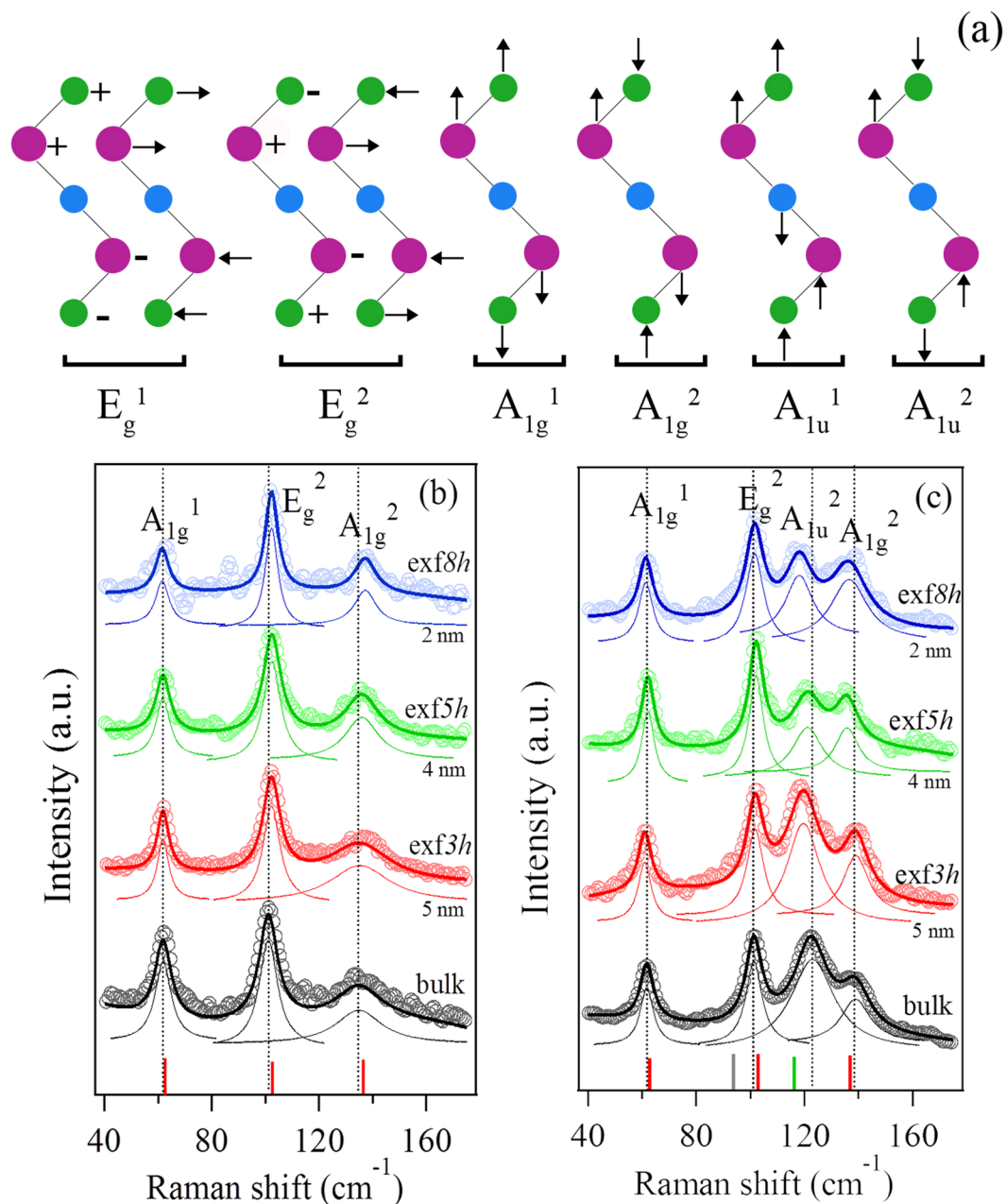
Figure 4. Vibration modes and Raman measurement. (**a**) Schematic diagram of the four Raman-active modes and two IR-active modes of the Bi_2Te_3 quintuple. The purple, blue and green colors represent the Bi, Te^2 and Te^1 atoms respectively. The vertical arrows represent out of plane vibration. The horizontal arrows represent in plane vibration that parallel to the page. The $-$, $+$ signs represent in plane vibrations that are perpendicular to the page. (**b,c**) Micro-Raman spectra of n-type $Bi_2Te_{2.7}Se_{0.3}$ without and with the presence of the A_{1u}^2 mode as function of different exfoliation times compared to the bulk sample. The open symbols represent the raw data and the solid lines through the raw data are the fits. The individual Lorentzian fits are shown below each spectrum. The red bars indicate the position of the optical phonon peaks of bulk n-type $Bi_2Te_{2.7}Se_{0.3}$. The gray (green) bar in (**c**) indicate the peak position of the IR-active A_{1u}^1 (A_{1u}^2) mode in bulk Bi_2Te_3.

Bulk n-type $Bi_2Te_{2.7}Se_{0.3}$ is known to exhibit four signature Raman-active optical phonons as shown in Fig. 4. Of these four modes, the lowest frequency E_g^1 mode was difficult to resolve owing to the increasing spectral background below $40\,cm^{-1}$. The other three modes[21] are centered at around $62.4\,cm^{-1}$ (A_{1g}^1), $102.6\,cm^{-1}$ (E_g^2) and $136.5\,cm^{-1}$ (A_{1g}^2) as represented by the red vertical bars in the spectra in Fig. 4b and c. Two types of Raman spectra were observed at various spots from all samples irrespective of the exfoliation time: those that exhibited the three modes mentioned above (Fig. 4b), and those that exhibited an additional peak at $\sim122\,cm^{-1}$ (Fig. 4c). The additional peak is an IR-active mode (A_{1u}^2) that has been reported previously[16,29–32], in nanoscale pristine Bi_2Te_3 (mode at around $116\,cm^{-1}$ indicated by the green vertical bar in Fig. 4c). We attribute the presence of the

A_{1u}^2 mode to symmetry breaking, possibly arising from the disorder induced by exfoliation and/or Se-dopant at the Te sites (Te^1 and Te^2), where Te^2 is the inversion center of the crystal symmetry (see Supplementary Fig. S1)[33]. As Se is lighter than Te, A_{1u}^2 mode was found blueshifted to ~122 cm^{-1} compared to the corresponding peak frequency in bulk Bi$_2$Te$_3$ (Fig. 4c), confirming the presence of Se. Several dozen spots were scanned, and A_{1u}^2 mode was observed in the Raman spectra at roughly half of these spots, as can be seen in the 2D Raman intensity maps in supplementary Fig. S5. The random occurrence of the A_{1u}^2 mode suggests variations in the structure of the exfoliated sheets, possibly from cleaving of the layers into sub-quintuples, as discussed further below. The other low wave number IR-active mode (A_{1u}^1) at ~94 cm^{-1} [34] (mode indicated by the gray vertical bar in Fig. 4c) in Bi$_2$Te$_3$ could not be discerned as this peak's frequency is close to that of the E_g^2 mode. Moreover, the A_{1u}^1 mode frequency may have blueshifted and as a result could be masked by the E_g^2 mode.

We next discuss the frequency and linewidth dependence of the modes shown in Fig. 5 as a function of inverse thickness of the samples. Figure 5a and c (Fig. 5b and d) show the mode frequency and linewidth dependences, respectively, in the absence (presence) of the A_{1u}^2 mode in the Raman spectra. In Fig. 5a and b, the A_{1g}^1 stretching mode frequency exhibited the least dependence on $1/t$ while the E_g^2 pinch mode frequency increased slightly with increasing $1/t$. Their linewidth dependences were relatively weaker than that exhibited by A_{1g}^2 and A_{1u}^1 modes. A_{1g}^2 mode is most sensitive to $1/t$: its frequency blueshifted by ~3 cm^{-1} in Fig. 5a while it redshifted in Fig. 5b and exhibited a significant sharpening from ~21 to 7 cm^{-1} with increasing $1/t$ (decreasing thickness). A blueshift of the A_{1g}^2 peak frequency with decreasing layer thickness was also reported by Zhao et al.[35] for CVD-grown pristine Bi$_2$Te$_3$ (inset in Fig. 5a) although it was accompanied by a broadening of the peak.

The discrepancy between our results and those from Zhao et al. can be explained by considering the effect of Se. The A_{1g}^2 phonon mode in Bi$_2$Te$_3$ exhibits strong electron phonon coupling (EPC), which becomes stronger with doping[36]. The strong EPC is also responsible for the formation of a Kohn anomaly at the Brillouin zone center and the observation of Dirac fermions in the topological surface states[37]. For a phonon with strong EPC, the anharmonic contribution to phonon decay is dwarfed by decay into electron hole pairs. However, in doped systems where the Fermi level is greater than the phonon energy, Pauli blocking reduces the number of electron states for the phonon to decay into, resulting in a longer phonon lifetime. This is manifested as a sharpening of the Raman peak. In addition, doping-induced change in the Fermi surface moves the Kohn anomaly away from the center of the Brillouin zone, where Raman active phonons are probed, and consequently causes a stiffening of the phonon mode. Indeed such observations have been made in doped graphene and metallic carbon nanotubes[38–40], where the E_g^2 mode (G peak) blueshifts and sharpens upon both hole and electron doping. While the observations of strong EPC and Kohn anomaly in n-type Bi$_2$Te$_3$ have been made only at low temperatures (<20 K), it is possible that the C/ME process breaks apart the Bi$_2$Te$_{2.7}$Se$_{0.3}$ layers into Se-doped quintuples where Se is substituted at the Te^2 sites in the Bi$_2$Te$_3$ quintuple, maintaining the crystal symmetry. In that case one could expect an increase in surface states especially with decreasing layer thickness, consistent with our observation of blueshifted peak frequencies (Fig. 5a) and decreasing linewidths of the A_{1g}^2 mode (Fig. 5c) with its strong EPC. This result also corroborates the increase in electron densities and formation of charged boundaries surmised from the transport measurements shown in Fig. 3.

Conversely, in the spectra where the A_{1u}^2 mode was observed (Fig. 4c), the A_{1g}^2 peak exhibited a redshift (by ~4 cm^{-1}) and broadening (by ~5 cm^{-1}), opposite to the trends seen in the spectra in which the A_{1u}^2 mode was absent. As mentioned above, the appearance of the A_{1u}^2 mode is attributed to breaking of crystal symmetry from the C/ME process. In this case it is possible that the C/ME process caused individual quintuples to fragment into sub-quintuples and the appearance of the A_{1u}^2 mode is induced by the disorder caused by this fragmentation. Due to spot-to-spot variations we did not observe any dependence of the A_{1u}^2 mode intensity on $1/t$. The Raman modes did exhibit broadening (by ~2–4 cm^{-1}) with increasing $1/t$ in the spectra when the A_{1u}^2 mode was present in the spectra (Fig. 5d). A decrease in the sample thickness typically leads to broadening of peaks, and such a broadening was indeed observed in the A_{1g} peaks with decreasing Bi$_2$Te$_3$ layer thickness by Zhao et al.[35]. The observation of disorder-induced IR active modes supports our thermal measurements on the exfnh-SPS samples, where κ reduced compared to the bulk value with increasing exfoliation time.

Based on the Raman and transport measurements, a new picture of the structural changes that occur in the C/ME processed Bi$_2$Te$_{2.7}$Se$_{0.3}$ crystal emerges: i) Se dopants preferably substitute for Te^2 sites followed by Te^1 sites, ii) during the chemical exfoliation process, the bond cleavages at various locations as depicted schematically in Fig. 6 (viz., Bi-Se or Bi-Te^1 bond) to form different sub-quintuples such as Te^1-Bi-Se^2, Te^1-Bi-Te^2, Bi-Te^1 and Bi-Se^1, and iii) the co-existence of quintuples and sub-quintuples in the exfoliated samples (as evidence directly by AFM and indirectly by micro-Raman studies described in Figs 2 and 4), promotes the formation of charged grain boundaries during SPS treatment. The charged grain boundaries leading to the transport properties discussed in Fig. 3.

Conclusion

In this study we presented systematic TE properties of few layered n-type Bi$_2$Te$_{2.7}$Se$_{0.3}$ produced by C/ME-SPS process. The TE measurements showed an increase (decrease) in carrier concentration (resistivity and thermal conductivity), accompanied by a mitigation of bipolar effect in α in the exfnh-SPS samples. Systematic AFM and micro-Raman studies of C/ME processed samples provided evidence for the co-existence of quintuples and sub-quintuples, which upon SPS process promote the formation of charged grain boundaries. Specifically, micro-Raman analysis revealed two types of spectra, which exhibited different frequency and linewidth trends as a function of layer thickness. The first set of spectra provided evidence for scattering from Se-doped quintuples, where the increased EPC leads to stiffening and sharpening of the A_{1g}^2 phonon. In the second set of spectra the disorder-induced IR-active mode A_{1u}^2 was evident, which we attribute to the formation of sub-quintuples caused by the C/ME process.
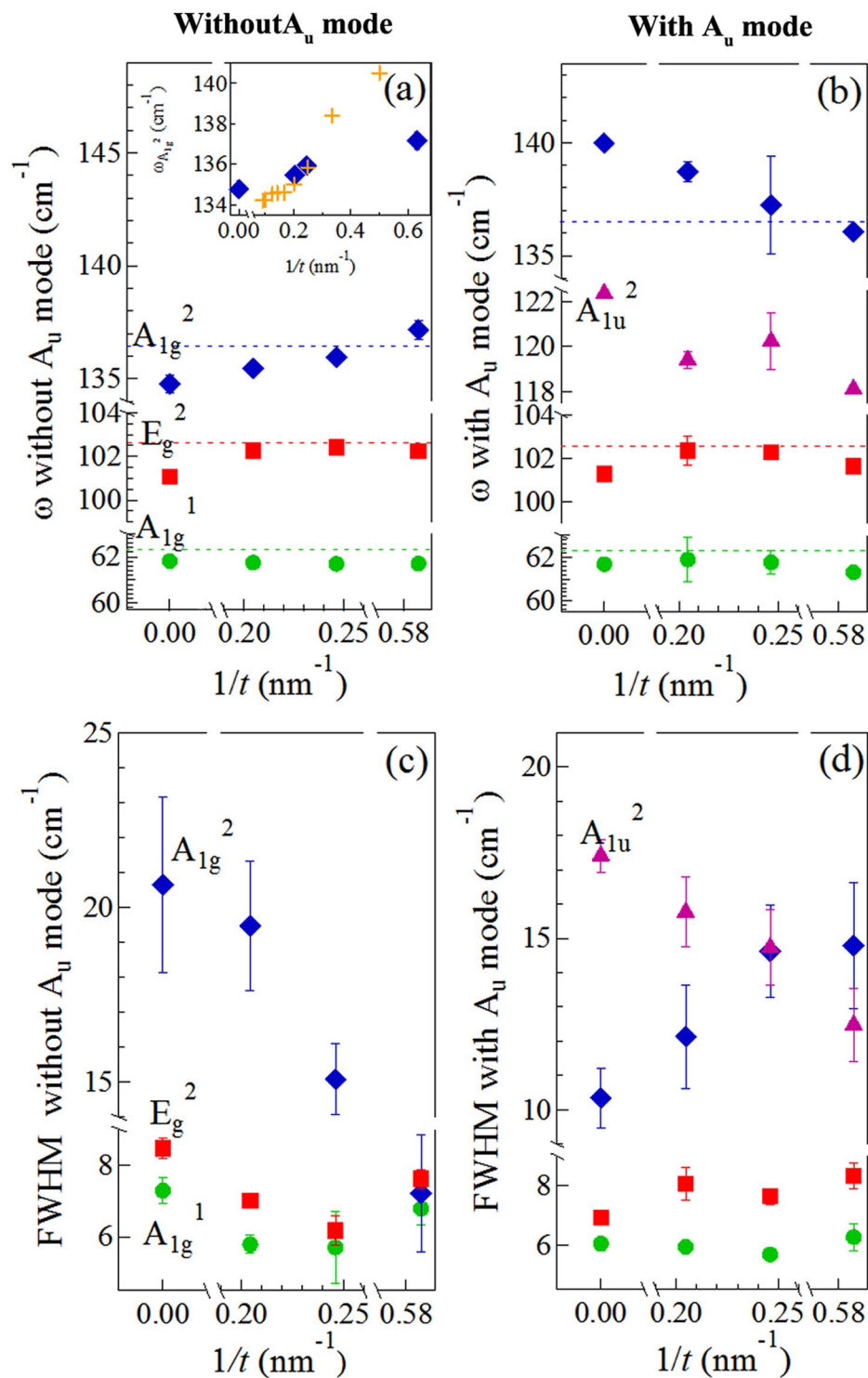
Figure 5. Frequency and FWHM dependence of $1/t$. (**a**) Dependence of the A_{1g}^1, E_g^2, A_{1g}^2 mode frequencies as a function of $1/t$ when the A_u mode is absent. Inset compares the A_{1g}^2 mode frequency ($+$) from Zhao *et al.*[35] with current work. (**b**) Dependence of the A_{1g}^1, E_g^2, A_{1g}^2 and A_{1u}^2 mode frequencies as a function of $1/t$. The dashed horizontal lines in (**a**) and (**b**) represent the peak frequencies of Raman modes in bulk *n*-type $Bi_2Te_{2.7}Se_{0.3}$. Change in linewidths (FWHM) of the A_{1g}^1, E_g^2, A_{1g}^2 modes as a function of $1/t$ (**c**) when the A_{1u}^2 mode is absent, (**d**) when the A_{1u}^2 mode is present.

Methods

Sample preparation. Pieces of *n*-type $Bi_2Te_{2.7}Se_{0.3}$ ingot (Marlow Industries, USA) were dispersed in N-methyl-2-pyrrolidinone (NMP) with a ratio of $10\,g/L$ and sonicated using 1/8-inch tip sonicator (Branson 250) at $20\,W$ for 0, 3, 5 and 8 hrs to obtain $Bi_2Te_{2.7}Se_{0.3}$ flakes. Subsequently, the supernatant solution was centrifuged at
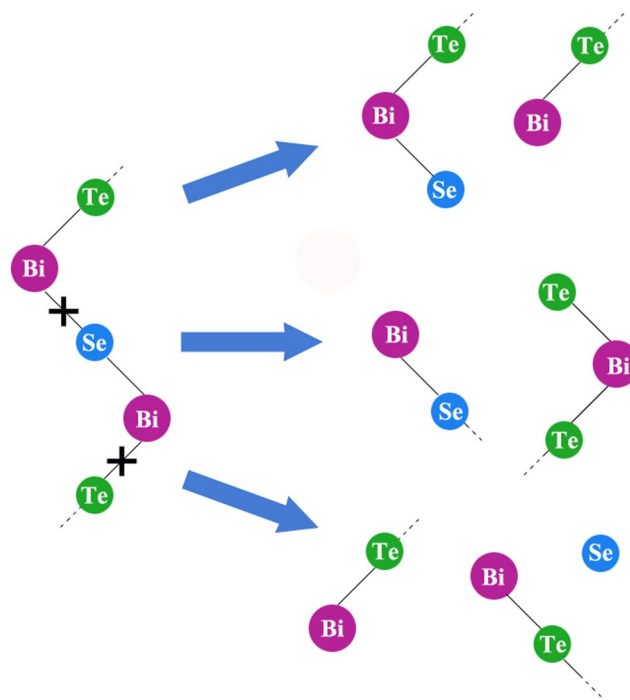
Figure 6. Schematic depiction of sub-quintuples formed as a result of the C/ME process.

4000 rpm for 2 hrs and the resulting powder was washed several times using deionized water to remove residual NMP and then oven dried at ~100 °C. Next, the exf*nh* flakes were compacted using spark plasma sintering (SPS, Dr. Sinter LabH-515S system) by loading ~2–3 g of exf*nh* into graphite dies and sintered at 500 °C for 5 minutes at an applied pressure of 30 MPa under a dynamic vacuum. The resulting SPS pellets were 12.5 mm in diameter and 2–3 mm in thickness, and a density of ~98–99% of the theoretical density. We refer to the SPS densified exf*nh* and commercial *n*-type Bi_2Te_3 ingot samples as exf*nh*-SPS and bulk, respectively.

Characterization. The thicknesses of the exf*nh* flakes were measured using non-contact mode atomic force microscopy (AFM, Model: AIST-NT Smart SPM, Micromasch cantilevers HQ: NSC14/Al BS-50). The average thickness was statistically calculated from the AFM height measurements conducted on 200–400 flakes for each exf*nh* sample. In addition, two-pass Kelvin probe force microscopy (KPFM, Micromasch conductive AFM probes HQ:NSC14/Cr-Au, scan rate: 1.0 Hz) was used for imaging and measuring the contact potential difference between the AFM tip and the sample at the charged grain boundaries. For each scan line, during the two-pass KPFM measurement, the height profile was recorded as AFM topographic image and followed by lifting the probe by 30 nm above the surface to measure the potential offset. The AIST-NT image analysis and processing software (Version 3.2.14) was used for AFM topographic and KPFM image analysis. The microstructural and chemical analyses were performed using the conventional transmission electron microscopy (TEM, Hitachi H7500) and high resolution X-ray diffraction (HR-XRD, RIGAKU Ultima IV diffractometer, Cu Kα radiation, $\lambda = 1.5406$ Å). Micro-Raman spectroscopy of exf*nh* samples was performed using a 633 nm excitation in a Renishaw Raman microscope equipped with a 100x objective lens (600 nm spot size). A reduced laser power (~100 μW) was used to prevent the inadvertent overheating of the exf*nh* flakes during the collection of their Raman spectra. Similar micro-Raman measurements were performed on the exf*nh*-SPS samples but the shiny surfaces of these samples did not yield a good Raman signal.

All transport measurements were performed in the perpendicular direction to the SPS pressing direction. The temperature dependent (15 to 300 K) resistivity and thermopower were measured quasi-simultaneously using a 4-probe measurement technique which is described in detail elsewhere[41]. The commercial ZEM (ULVAC-RIKO, ZEM-2) was used to measure resistivity and thermopower from 300–500 K under partial He-atmosphere. The thermal conductivity (κ_T) was measured from 20–320 K, using a standard steady-state technique on a custom designed measurement system[42]. The high temperature thermal conductivity was calculated using the relation $\kappa_T = C_P D d$; where d is the packing density of the material, D the thermal diffusivity and C_P ($\approx C_V$, for solids) the specific heat capacity. The heat capacity was measured using a NETZSCH DSC 404C, thermal diffusivity was measured using a NETZSCH LFA 457 system and the packing density was measured by the Archimedes' principle. Since the laser flash measures the thermal diffusivity along the SPS pressure direction, whereas the low temperature transport properties are measured along the direction perpendicular to SPS direction (in the plane of pellet), several bars of our samples were cut and re-stuck together after rotating the bars by 90 degrees using JB Weld (a thermally conducting and electrically insulating glue), in order to measure all the properties along the same direction. Both the electronic and thermal transport measurements in the low and high temperature regimes were in good agreement over the entire temperature range of 15–500 K. The carrier concentration was determined from 10–300 K by Hall coefficient measurements using the commercial Quantum Design Physical Properties Measurement System (PPMS) under a magnetic field sweep of 5 kOe.

References

1. Scherrer, S & Scherrer, H. Bismuth Telluride, Antimony Telluride, and Their Solid Solutions. In Rowe, D. M. (ed.) *CRC Handbook of thermoelectrics*, chap. 19, 211–238 (New York, 1995).
2. Disalvo, F. J. Thermoelectric Cooling and Power Generation. *Science* **285**, 703–706 (1999).
3. Bell, L. E. Cooling, Heating, Generating Power, and Recovering Waste Heat with Thermoelectric Systems. *Science* **321**, 1457–1461 (2008).
4. Lukas, M., Casper, F. & Yan, B. Topological insulators and thermoelectric materials. *Physica Status Solidi–Rapid Research Letters* **7**, 91–100 (2013).
5. Ghaemi, P., Mong, R. S. K. & Moore, J. E. In-Plane Transport and Enhanced Thermoelectric Performance in Thin Films of the Topological Insulators Bi_2Te_3 and Bi_2Se_3. *Physical Review Letters* **166603**, 1–4 (2010).
6. Osterhage, H. *et al*. Thermoelectric properties of topological insulator Bi_2Te_3, Sb_2Te_3, and Bi_2Se_3 thin film quantum wells. *Applied Physics Letters* **105**, 1–5 (2014).
7. Hicks, L. D. & Dresselhaus, M. S. Thermoelectric figure of merit of a one-dimensional conductor. *Physical Review B* **47**, 16631–16634 (1993).
8. Xie, W., Tang, X., Yan, Y., Zhang, Q. & Tritt, T. M. Unique nanostructures and enhanced thermoelectric performance of melt-spun BiSbTe alloys. *Applied Physics Letters* **94**, 1-3 (2009).
9. Poudel, B. *et al*. High-thermoelectric performance of nanostructured bismuth antimony telluride bulk alloys. *Science (New York, N.Y.)* **320**, 634–638 (2008).
10. Puneet, P. *et al*. Preferential scattering by interfacial charged defects for enhanced thermoelectric performance in few-layered n-type Bi_2Te_3. *Scientific Reports* **3**, 1–7 (2013) doi: 10.1038/srep03212.
11. Lee, M. J. *et al*. Thermoelectric materials by using two-dimensional materials with negative correlation between electrical and thermal conductivity. *Nature Communications* **7**, 1–7 (2016).
12. Sun, Y. *et al*. Atomically Thick Bismuth Selenide Freestanding Single Layers Achieving Enhanced Thermoelectric Energy Harvesting. *J. Am. Chem. Soc.* **134**, 20294–20297 (2012).
13. Hippalgaonkar, K. *et al*. Record High Thermoelectric Powerfactor in Single and Few-Layer MoS_2. arXiv:1505.06779 (2015).
14. Soni, A. *et al*. Enhanced Thermoelectric Properties of Solution Grown $Bi_2Te_{3-x}Se_x$ Nanoplatelet Composites. *Nano Letters* **12**, 1203–1209 (2012).
15. Russo, V. *et al*. Raman spectroscopy of Bi-Te thin films. *Journal of Raman Spectroscopy* **39**, 205–210 (2008).
16. Teweldebrhan, D., Goyal, V. & Balandin, A. A. Exfoliation and characterization of bismuth telluride atomic quintuples and quasi-two-dimensional crystals. *Nano Letters* **10**, 1209–1218 (2010).
17. Goyal, V., Teweldebrhan, D. & Balandin, A. A. Mechanically-exfoliated stacks of thin films of Bi_2Te_3 topological insulators with enhanced thermoelectric performance. *Applied Physics Letters* **97**, 133117 (2010).
18. Satterthwaite, C. B. & Ure, R. W. Electrical and Thermal Properties of Bi_2Te_3. *Physical Review* **108**, 1164–1170 (1957).
19. Drabble, J. R. & L. Goodman, C. H. Chemical Bonding in Bismuth Telluride. *Journal of Physics and Chemistry of Solids* **5**, 142–144 (1958).
20. Shahil, K. M. F., Hossain, M. Z., Goyal, V. & Balandin, A. A. Micro-Raman spectroscopy of mechanically exfoliated few-quintuple layers of Bi_2Te_3, Bi_2Se_3, and Sb_2Te_3 materials. *Journal of Applied Physics* **111**, 1–8 (2012).
21. Richter, W. & Becker, C. R. A Raman and far-infrared investigation of phonons in the rhombohedral V_2-VI_3 compounds. *Physica Status Solidi (B)* **84**, 619–628 (1977).
22. Degarmo, E. P., T., B. J. & Kohser, R. A. *Materials and Processes in Manufacturing*, 11th edition edn (Wiley, 2012).
23. Cutler, M., Leavy, J. F. & Fitzpatrick, R. L. Electronic transport in semimetallic cerium sulfide. *Physical Review* **133**, A1143–A1152 (1964).
24. Snyder, G. J. & Toberer, E. S. Complex thermoelectric materials. *Nature materials* **7**, 105–114 (2008).
25. Goldsmid, H. J. & Sharp, J. W. Estimation of the Thermal Band Gap of a Semiconductor from Seebeck Measurements. *Journal of Electronic Materials* **28**, 869–872 (1999).
26. Seto, J. Y. The electrical properties of polycrystalline silicon films. *Journal of Applied Physics* **46**, 5247–5254 (1975).
27. Martin, J., Wang, L., Chen, L. & Nolas, G. Enhanced seebeck coefficient through energy-barrier scattering in PbTe nanocomposites. *Physical review B* **79**, 115311 (2009).
28. Mehta, R. J. *et al*. A new class of doped nanobulk high-figure-of-merit thermoelectrics by scalable bottom-up assembly. *Nature Materials* **11**, 233–240 (2012).
29. Shahil, K. M. F., Hossain, M. Z., Teweldebrhan, D. & Balandin, A. A. Crystal symmetry breaking in few-quintuple Bi_2Te_3 films: Applications in nanometrology of topological insulators. *Applied Physics Letters* **96**, 1–4 (2010).
30. Giri, L., Mallick, G., Jackson, A. C., Griep, M. H. & Karna, S. P. Synthesis and characterization of high-purity, single phase hexagonal Bi_2Te_3 nanostructures. *RSC Advances* **5**, 24930–24935 (2015).
31. Liang, Y. *et al*. Raman scattering investigation of Bi_2Te_3 hexagonal nanoplates prepared by a solvothermal process in the absence of NaOH. *Journal of Alloys and Compounds* **509**, 5147–5151 (2011).
32. Liang, Y. *et al*. The effect of the Bi source on optical properties of Bi_2Te_3 nanostructures. *Solid State Communications* **151**, 704–707 (2011).
33. Jenkins, J., Rayne, J. & Ure, R. Elastic Moduli and Phonon Properties of Bi_2Te_3. *Physical Review B* **6**, 3171–3184 (1972).
34. Yuan, J. *et al*. Raman Spectroscopy of Two-Dimensional $Bi_2Te_xSe_{3-x}$ Platelets Produced by Solvothermal Method. *Materials* **8**, 5007–5017 (2015).
35. Zhao, Y. Y. *et al*. Interlayer vibrational modes in few-quintuple-layer Bi_2Te_3 and Bi_2Se_3 two-dimensional crystals: Raman spectroscopy and first-principles studies. *Physical Review B* **90**, 1–8 (2014).
36. He, J. *et al*. Tunable Dirac Fermion Dynamics in Topological Insulators. *Sci. Rep.* **3**, 1–6 (2013).
37. Kondo, T. *et al*. Anomalous Dressing of Dirac Fermions in the Topological Surface State of Bi_2Se_3, Bi_2Te_3, and Cu-Doped Bi_2Se_3. *Physical Review Letters* **110**, 1–5 (2013).
38. Pisana, S. *et al*. Breakdown of the adiabatic Born-Oppenheimer approximation in graphene. *Nature materials* **6**, 198–201 (2007).
39. Yan, J., Zhang, Y., Kim, P. & Pinczuk, A. Electric Field Effect Tuning of Electron-Phonon Coupling in Graphene. *Physical Review Letters* **98**, 1–4 (2007).
40. Lazzeri, M., Piscanec, S., Mauri, F., Ferrari, A. C. & Robertson, J. Phonon linewidths and electron-phonon coupling in graphite and nanotubes. *Physical Review B* **73**, 1–6 (2006).
41. Pope, A. L., Littleton, R. T. & Tritt, T. M. Apparatus for the rapid measurement of electrical transport properties for both "needle-like" and bulk materials. *Review of Scientific Instruments* **72**, 3129–3131 (2001).
42. Pope, A. L., Zawilski, B. & Tritt, T. M. Description of removable sample mount apparatus for rapid thermal conductivity measurements. *Cryogenics* **41**, 725–731 (2001).

Acknowledgements

Author Contributions

F.L. and M.K. contributed towards the samples exfoliation process, L.H. conducted the A.F.M. measurements, P.P. performed S.P.S. and measured thermoelectric properties, R.R. and F.L. performed the Raman spectroscopy measurements and data analysis, S.B., F.L. and R.R. analyzed the results. R.P. and A.M.R. reviewed the results and the manuscript.

Additional Information

Supplementary information accompanies this paper at https://doi.org/10.1038/s41598-017-16479-y.

Competing Interests: The authors declare that they have no competing interests.

Publisher's note: Springer Nature remains neutral with regard to jurisdictional claims in published maps and institutional affiliations.